DOI: 10.1002/((please add manuscript number))
Article type: Full paper

High efficiency all-dielectric metalenses for mid-infrared imaging

Haijie Zuo, Duk-Yong Choi, Xin Gai, Pan Ma, Lei Xu, Dragomir N. Neshev, Baoping Zhang, and Barry Luther-Davies*

H. Zuo, Dr. D. Choi, Dr. X. Gai, Dr. P. Ma, Prof. B. Luther-Davies
Centre for Ultrahigh bandwidth Devices for Optical Systems, Laser Physics Centre, Research School of Physics and Engineering, The Australian National University, Canberra, ACT 2601, Australia
E-mail: duk.choi@anu.edu.au
Dr. L. Xu, Prof. D. N. Neshev
Nonlinear Physics Centre, Research School of Physics and Engineering, The Australian National University, Canberra, ACT 2601, Australia
H. Zuo, Prof. B. Zhang
Laboratory of Micro/Nano Optoelectronics, Department of Electronic Engineering, Xiamen University, Xiamen 361005, Fujian, China

Keywords: metasurfaces, mid-infrared imaging, hydrogenated amorphous silicon (α-Si:H)

Abstract

Metasurfaces-based flat optics, which can make use of existing foundry planar technology for high throughput production, allows the arbitrary control of the wavefront and polarization of light within sub-wavelength thick structures. So far, however, flat optics for the mid-infrared has received far less attention than devices operating at visible or near-infrared wavelengths. Here, we demonstrate polarization-insensitive, highly efficient, all-dielectric metalenses operating in the mid-infrared (MIR) around 4μm. The metalens was designed using rigorous coupled wave analysis and was based on hydrogenated amorphous silicon (α-Si:H) nano-pillars supported by a MgF_2 substrate. The metalenses produced close to a diffraction-limited focal spot and could resolve structures on the wavelength-scale where the focusing efficiency reached

78% at magnification of ×120. The imaging qualities were comparable with commercial bulk-molded chalcogenide aspheric lenses. Our results provide novel solutions for existing MIR technology and nurture new functionalities with the population of miniaturized and planarized opto-electrical devices.

1. Introduction

Planar all-dielectric metasurfaces permit the arbitrary control of the wavefront and polarization within sub-wavelength thick structure at the surface whilst remain highly efficient [1–4]. Benefitting from their compact configuration and fabrication using the advanced capabilities of CMOS foundries, metasurface optics have unprecedented advantages over their traditional bulky and expensive counterparts [3,5–7]. The first optical devices based on metasurfaces consisted of metal nano-antenna-like plasmonic scatters [8–11], however, these suffered from low efficiency due to their high ohmic losses. In contrast, all-dielectric metasurfaces are based on optical Mie-type resonances, and as a result the absorption loss of the sub-wavelength thick layer from which they are fabricated can be negligible. Based on this concept various optical components operating in transmission with high efficiency have been demonstrated, including gratings [12], lenses [13–16], beam shapers [3,17,18], deflectors [19] and holograms [6,7,20].

Metalenses highlight the potential of this planar technology and can respond to the growing demand for miniaturization of conventional imaging lenses for portable and wearable electronic devices, computer vision, microscopy, etc. A variety of dielectric metalenses based on different structures have been demonstrated and their focusing characteristics studied [13,21–23]. Recently,

metalenses for visible light were shown to be capable of sub-wavelength resolution and high optical efficiency resulting in performance comparable with commercial objective lenses [15]. Moreover, the direct integration of a metalenses doublet onto a CMOS image sensor has demonstrated the ability to achieve sophisticated image corrections in a compact configuration [16]. Most of results to date, however, have focused on visible or near-infrared, and little has been reported on metaoptics for the MIR, which is far less developed than that of shorter wavelengths. This has been mainly due to the limited availability of high refractive index layers on MIR-transparent substrates, less advanced manufacturing technology, and expensive characterization techniques. On the other hand, the longer wavelengths in the MIR relax the constraints on fabrication accuracy compared with the case of metalenses designed for the visible. This allows the application of lower-resolution photolithographic processes rather than expensive deep UV steppers or high resolution electron beam writers which is inevitable for pattering a metalens operating in the visible. Furthermore the relative immaturity of conventional optics for the MIR compared with their visible counterparts provides an opportunity to create compact, efficient and low cost MIR metalenses, which will substantially advance the existing MIR technology and can be readily applied in various fields ranging from thermal imaging; surveillance; molecular fingerprint detection for anti-terrorism, drug diagnostic; micro-spectroscopy; etc.

In this work, we demonstrated experimentally a novel, highly efficient material platform suitable for the fabrication of MIR metasurfaces. The metasurface itself consisted of a periodic arrangement of nano-pillars (NPs), which provide spatially-dependent phase modulation at

subwavelength spatial sampling resolution resulting from the localized resonant nature of the underlying dielectric resonators [13,24,25]. We demonstrate that our metalenses focus MIR light to close to a diffraction-limited focal spot and that their imaging qualities are comparable to those of commercial aspheric bulk-molded chalcogenide glass MIR lenses. The aberration factors of the metalenses were studied to identify possible further improvement of the performance via the refinement of fabrication process or the application of a doublet corrected for chromatic aberrations [16,22,23].

Several dielectric material platforms with various resonant structures have been employed as the building blocks for metalenses operating in the visible and near-infrared with ever-increasing transmission efficiency. These include metalenses based on crystalline silicon (c-Si)[21]; poly-silicon on a quartz substrate[3]; hydrogenated amorphous silicon (α-Si:H) on silica[13,16]; and most recently, TiO_2 nanofin on glass[15]. However, these platforms are unsuitable for efficient MIR devices because of the poor transparency of substrate materials such as SiO_2 in the MIR or the high reflection loss from silicon. For the MIR, metalenses based on c-Si[21] and metallic plasmonics[26] have been proposed but suffer from the fundamental limits stated above. In this work, we developed a metasurface based on an array of α-Si:H NPs supported on a double-side polished MgF_2 substrate. This structure takes advantages of the negligible absorption of the α-Si:H thin film in the MIR and high refractive index difference between rod resonators (n~3.5) and the MgF_2 substrate (n~1.37), which leads to localized optical resonance induced by strong field confinement within the NPs. Furthermore, unlike the work reported in [4, 15] where the phase profile was created by a relative rotation of each nanofin

resonator thus making the metalens polarization-sensitive so it operated only with circularly polarized light, here the circularly symmetric resonance properties of NP resonators made our metalenses polarization-insensitive and unlocks wider applications in general imaging optics compared with previous reports [3,8,15,27,28].

2. Metalens design

Instead of a square lattice, we used a hexagonal pattern because it is the densest planar packing arrangement. This leads to smoother sampling of the phase near the boundary of each zone and results in better performance compared with the case of a square lattice. The silicon NPs were placed at the centers of each hexagonal unit cell. We simulated the transmission properties of these metasurfaces using the rigorous coupled-wave analysis (RCWA) method [29, 30]. RCWA is a frequency-domain modal method based on the decomposition of the periodic structure and the pseudo-periodic solution of Maxwell's equations in terms of their Fourier series expansions. The field is discretized upon the Fourier basis along transverse periodic directions, and is expressed analytically along the other propagation direction. RCWA has been widely used for modelling periodic optical structures due to its fast convergence and accurate far-field calculations. We examined the transmission properties of our periodic system of NPs with different radius and period instead of studying the response of an isolated NP. Such characterization provides a very good approximation of the local transmission properties of high-index metasurface composed of gradually varying NPs. The performance of designed metasurface is insensitive to the polarization of the incident beam due to the symmetry of the

NP structure, and thus the output wave possesses the same polarization state as the input wave. The design of the metalens used in transmission mode is shown schematically in Figure 1a. A converging wavefront generated by the high aspect ratio NPs (the structure parameters are shown in Figure 1c) can be described by **Equation 1,**

$$\Phi(r) = \frac{2\pi}{\lambda}\left(f - \sqrt{r^2 + f^2} \right) \tag{1}$$

where f is the lens focal length and λ is the wavelength of light. The phase delay and transmission as a function of NP radius and period for various heights (i.e. film thickness) were calculated using rigorous coupled-wave analysis (RCWA). Here, the NP height was chosen to be 2μm for sake of fabrication feasibility, and we employed a hexagonal lattice with a constant a=2μm, providing a sampling resolution of λ/2 at the design wavelength of 4μm. The dependence of the transmitted phase and amplitude as a function of NP radius, R, and lattice constant, a, are shown in Figure 1b, whilst **Figure S1** in the supporting materials shows how these parameters change with NP heights of 1, 1.5, and 2.5μm. The specific results for a=2μm and h=2μm are plotted in Figure 1d, which corresponds to the dashed lines in Figure 1b; It is evident from Figure 1d that the NPs offer full 2π phase coverage as the radius is changed from 100nm up to 600nm, whilst at the same time the transmission efficiency remains close to unity.

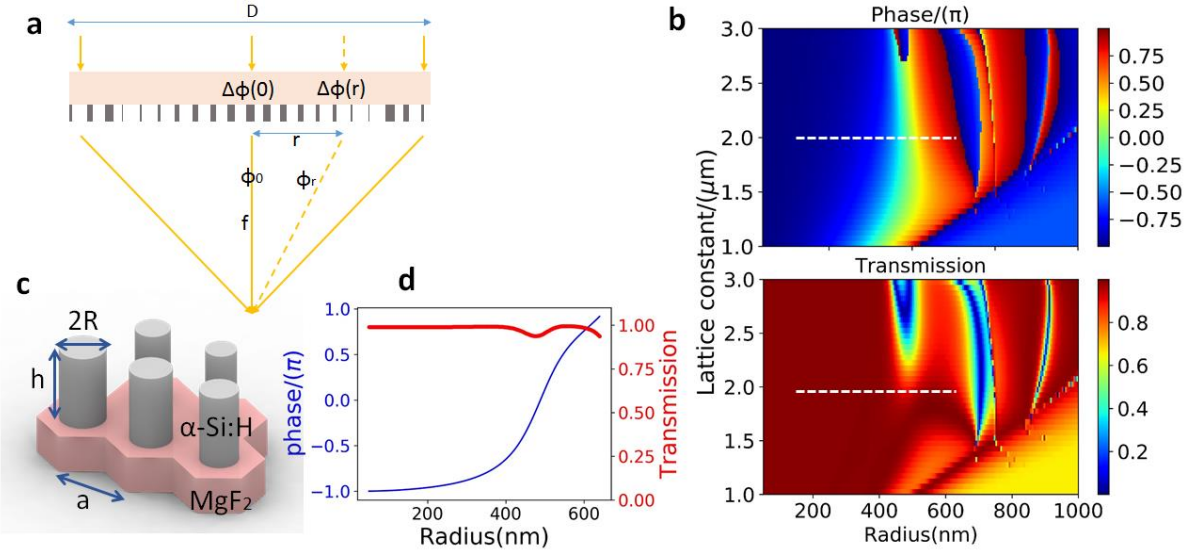

Figure 1. Design parameters for the MIR metalens working at 4μm wavelength. a) Configuration of MIR metalens and the calculation of phase propagation. b) Simulated phase delay and transmission as functions of the lattice constant and NP radius for a NP height of 2μm. c) Structure parameters of the NP unit cell: NP radius - R; height – h; and period - a. d) Calculated phase delay and transmission for h=2μm, a=2μm.

3. Numerical verification using beam deflector

In order to verify the feasibility of the metalens design numerically, a MIR beam deflector was designed by employing the relation from Figure 1d, which is a periodic structure and only one unit cell was modeled, requiring much less computation resources than the metalens. The slanted phase profile of a beam deflector was designed using a relation similar to Equation 1, and the 2D NP array was constructed and modeled by a 3D FDTD model [31] (FDTD Solution, Lumerical Solutions Inc.). As shown in **Figure 2**a, the wavefront of a plane wave was tilted when transmitted through the metasurface made from a similar NP array to the lens, and the deflection angle θ_t extracted from the FDTD calculation, accurately matches the design (Figure 2b). The deflection efficiency reached 96% for small angles (5°) but decreased to ~70% at an angle of 25° due to under-sampling of the rapidly varying phase profile that occurs at

larger deflection angles. This efficiency droop can be partially overcome by reducing the lattice constant of the NP array. A feasible approach using denser arrays to improve the response at larger angles is discussed in **Figure S2** in the supporting material. The accuracy of the deflected angle and high efficiency confirm the validity of the calculation of RCWA and the design procedure.

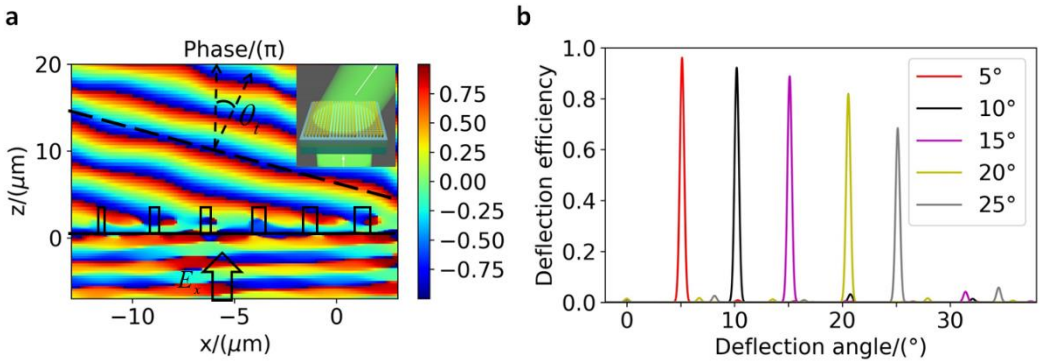

Figure 2. Simulation of a MIR(4μm) beam deflector based on a metasurface with similar parameters to the proposed metalens. a) Cross section of slanted phase profile generated by metasurface beam deflector; the inset shows the working configuration of the beam deflector. b) Deflection angle and corresponding efficiency.

4. Experimental fabrication and characterization of the metalenses

The fabrication of the MIR metalenses started with oxygen cleaning of a double-side polished MgF_2 substrate (c-cut) to promote the adhesion between the substrate and amorphous silicon film. Following this, a 2 μm thick α-Si:H film was deposited onto one side of the substrate by plasma-enhanced chemical vapor deposition (PECVD, Plasmalab 100 from Oxford) using optimized conditions in our previous work[32]. The film shows a negligible extinction coefficient (<0.001, measured by IR-VASE, JA Woollam, Inc.) over the wavelength range from 1.5 μm to 10 μm (see **Figure S3** in the supporting material). After spin-coating of an electron

beam resist (ZEP520A from Zeon Chemicals), a thin layer of e-spacer 300Z (Showa Denko) was applied to avoid charging during subsequent electron beam exposure. The NP pattern was then formed using an electron beam writer (EBL, Raith150) and subsequent development in ZED-N50. Next a 60 nm aluminum (Al) layer was deposited by e-beam evaporation (Temescal BJD-2000), followed by a lift-off process by soaking the sample in resist remover (ZDMAC from ZEON Co.). The remaining circular Al pattern array was used as the etch mask to transfer the designed pattern into the α-Si:H film using fluorine based inductively coupled plasma-reactive ion etching (ICP-RIE, Oxford Plasmalab System 100). The etching conditions were optimized to obtain a highly anisotropic etching profile for the α-Si:H. Finally, the residual Al etch mask was removed by chlorine-based plasma etching. The fabrication procedure is illustrated in **Figure S4** in the supporting material. **Figure 3** shows optical and SEM images of the produced metalens.

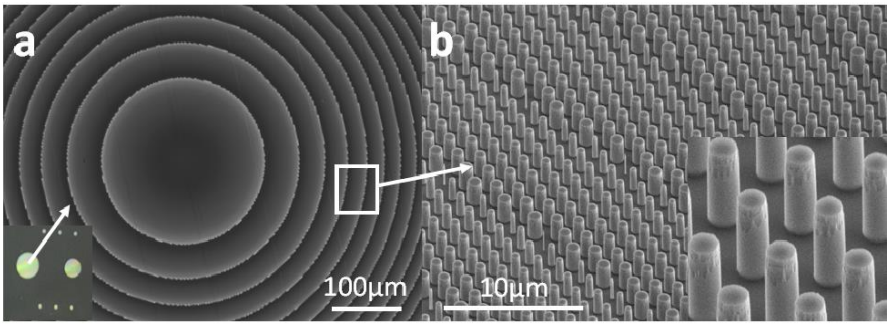

Figure 3. Characterization of MIR metalenses. a) Top view of central part of metalenses from an optical microscope. The insert shows the overall optical image of fabricated metalenses with different aperture size. b) Details of NPs of metalens from SEM imaging.

The optical properties were characterized using the configuration shown in **Figure S5**. A femtosecond mid-infrared optical parametric amplifier tunable from 3.3μm~4.6μm (Hotlight Systems MIROPA-*fs*) was used as the illumination source. The mid-infrared images were

recorded using an InSb camera (Xenics Onca MWIR-640). To evaluate the size of the focal spot and for the imaging tests (Figure S4a-b), an input lens with low numerical aperture (NA0.2) was defocused in the measurement setup to provide uniform illumination onto themetalens surface. We characterized the imaging resolution against a 1951 United States Air Force (USAF) resolution test chart which was obtained by patterning the chart into a 100 nm thick Al film deposited on a double-side polished silicon wafer. For the focusing efficiency measurement in Figure S5c, a metal pinhole with 20μm diameter (aperture 1) was inserted between input objective lens and the metalens. The transmission efficiency was then defined by the ratio of energy at the image at aperture 2 (which was selected with a variable iris with a size 2~3 times that of the imaging of the focal spot) compared with the energy transmitted through aperture 1 without the metalens in place. The relative power was measured using a large area PbSe detector. The stop next to the attenuator reduced the effective NA of the input objective to ensure that all the energy transmitted through aperture 1 was captured by the metalens.

5. Results and discussion

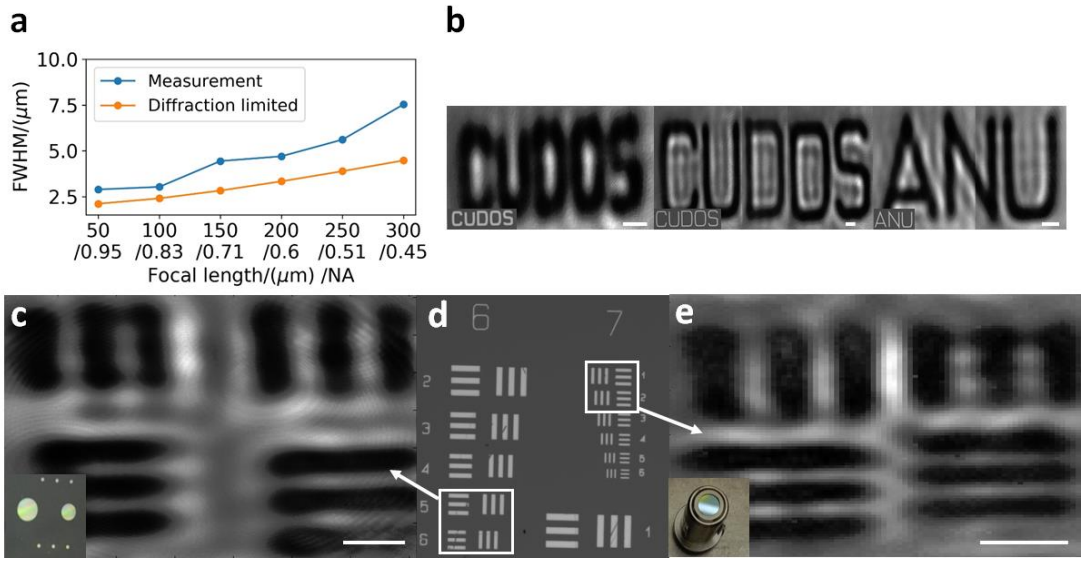

Figure 4. Optical characterization of MIR metalens using 4μm wavelegnth. a) FWHM of focal

spots from metalens with different numerical aperture. b) Examples of imaging using MIR metalenses, insets show corresponding imaged patterns under optical microscope. c) Resolution test chart imaged by MIR metalenses (insert). d) Optical image of resolution test chart, group 6 and 7. e) Resolution test chart imaged by a NA=0.54 molded aspheric chalcogenide lens (Thorlabs, insert). Scale bars, 10μm.

We fabricated a set of metalens with focal lengths from 300μm down to 50μm in 50μm steps and having a fixed diameter of 300μm which corresponded to NA values from 0.95 to 0.45. As is shown in **Figure 4**a, the measured FWHM's of the focal spots were close to the diffraction limit. Note that the actual FWHM should be smaller as numerical aperture of the output lens (NA0.56) used in the measurement setup (Figure S5a) was not matched accurately with the measured metalens. To evaluate the imaging performance, much larger metalenses were produced with both the diameter and the focal length being 2mm, which corresponds to a numerical aperture of 0.45. Figure 4b shows examples of imaging as demonstration using this metalens at a wavelength of 4μm. Here, the imaged sample was obtained by patterning letters with 100 nm thick Al film onto double-side polished silicon substrates, as shown in the insets of Figure 4b. Figure 4c displays the quantitative imaging resolution obtained by imaging 1951 USAF test chart using the setup in Figure S5b, where the metalenses operates at magnification of 120×. The finest features that the metalenses could clearly resolve was element 6 in group 6 (Figure 4d), which has a corresponding linewidth of 4.38μm and is equivalent to 114 line pairs per mm (lp/mm). For comparison, we repeated the measurement using a conventional molded chalcogenide lens with numerical aperture of 0.56 (C036TME-E, Thorlabs); the smallest linewidth resolved was element 2 in group 7 with a linewidth of 3.48μm, equals to 143 lp/mm. Noting the NA of the chalcogenide lens is ~10% larger than the metalenses (NA 0.45) used in

the same imaging setup, we can therefore conclude that the imaging resolution of the metalens is at least comparable with the these conventional molded MIR lenses. The metalens was tested with different linear polarizations and no difference in terms of imaging behavior was found between the measurements. This indicates that the lens is polarization-insensitive in agreement with the theoretical model of the radially symmetric resonators discussed in Part 2. We tuned the wavelength of MIR OPA from 3.7μm to 4.2μm, over which no noticeable degradation in the imaging resolution was observed when we tuned the working distance from the metalens to the resolution target accordingly (equal to changing focal length), which agrees with the theoretical model of the dispersive behaviour underlying the NP resonators with low quality factor, whose typical bandwidth is several percent of the design wavelength [6]. The focusing efficiency of the metalenses was measured to be ~78% using the setup in Figure S5c, which was 19% less than the estimate from the RCWA calculation (97%) shown in Figure 1d. Providing 2.5% of the Fresnel reflection loss from the MgF_2/air interface at the backside of metalenses, we attribute the extra ~16.5% loss to the fabrication imperfections, absorption of defects, and wavefront under-sampling due to the relatively large NP period as was predicted from the FDTD calculations of the beam deflector in Figure 2b. The focal length and focusing efficiency of the metalens are subject to chromatic dispersion, which can be corrected with approaches proposed and demonstrated in previous work [16, 23, 33]. Nevertheless, the current metalens can be readily employed in applications with laser or narrow-band light sources.

The imaging resolution measurement with the test chart agrees with the modulation transfer function (see **Figure S6** in supporting material), which was obtained from the Fourier transform

of the point spread function measured for the metalenses. The reduced performance compared with a diffraction-limited system comes partly from fabrication errors. For instance, the averaged radius of fabricated NPs was ~5% larger than the design across the entire metalens structure (see **Figure S7** in supporting material), and this imposes a different phase across the beam leading to a non-uniform RMS wavefront error. Apart from improving the precision of fabrication, the performance of the metalens could be further improved by employing an algorithm for phase optimization using optical design software such as ZEMAX (OpticStudio, Zemax LLC). Also, a metalens doublet could be applied in real imaging system as it allows sophisticated imaging corrections leading to a wide angle of view (AOV) and correction of chromatic aberrations.

6. Conclusion

In summary, we demonstrated a highly efficient all-dielectric metalenses operating in the MIR spectral region. An α-Si:H NP array supported by a MgF_2 substrate was employed as the building block for the metasurface. The large refractive index contrast between the resonators and the substrate led to strong optical resonances within the individual NPs, that allowed the desired phase modulation to be produced for the metalens in transmission. We calculated the phase and transmittance response as functions of the geometric parameters of the NPs using the RCWA, then numerically verified the performance by designing a MIR beam deflector. The fabricated metalenses produced focal spot size using a coherent source that was close to the diffraction limit. It was also demonstrated that MIR images could be resolved at the wavelength-scale and that the focusing efficiency was as high as 78%. The main deficiencies in the current

lenses have been discussed and further improvement have been identified. Nevertheless, the metalens was comparable in performance with commercial molded chalcogenide lenses, but have the advantages of a smaller footprint and negligible weight, making them attractive for deployment in weight sensitive applications such as satellite imaging. We note that the materials used in these metalenses are compatible with conventional CMOS processes, which enable not only high throughput at low-cost, but also a planar form factor favorable for on chip integration. As such, our work provides a novel solution for existing MIR optical imaging systems and nurture new functionalities aimed at miniaturized and planarized opto-electronic devices, which can substantially benefits the far less developed MIR optics.

Supporting Information
Supporting Information is available from the Wiley Online Library or from the author.

Acknowledgements
The authors acknowledges the facility support from the ANU node of the Australian National Fabrication Facility (ANFF). This work is supported by China Scholarship Council (201506310074); Australian Research Council (ARC) Future Fellowship (FT110100853); and the ARC Centre of Excellence for Ultrahigh Bandwidth Devices for Optical Systems (CE110001018).

Received: ((will be filled in by the editorial staff))
Revised: ((will be filled in by the editorial staff))
Published online: ((will be filled in by the editorial staff))

References

[1] A. I. Kuznetsov, A. E. Miroshnichenko, M. L. Brongersma, Y. S. Kivshar, B. Luk'yanchuk, *Science* **2016**, *354*, aag2472.

[2] I. Staude, J. Schilling, *Nat Photonics* **2017**, *11*, 274.

[3] D. M. Lin, P. Y. Fan, E. Hasman, M. L. Brongersma, *Science* **2014**, *345*, 298.

[4] R. C. Devlin, M. Khorasaninejad, W. T. Chen, J. Oh, F. Capasso, *Proc. Natl. Acad. Sci.* **2016**, *113*, 10473.

[5] J. P. B. Mueller, N. A. Rubin, R. C. Devlin, B. Groever, F. Capasso, *Phys. Rev. Lett.* **2017**, *118*, 113901.

[6] A. Arbabi, Y. Horie, M. Bagheri, A. Faraon, *Nat. Nanotechnol.* **2015**, *10*, 937.

[7] L. Wang, S. Kruk, H. Z. Tang, T. Li, I. Kravchenko, D. N. Neshev, Y. S. Kivshar, *Optica* **2016**, *3*, 1504.

[8] N. F. Yu, F. Capasso, *Nat. Mater.* **2014**, *13*, 139.

[9] N. F. Yu, P. Genevet, M. A. Kats, F. Aieta, J. P. Tetienne, F. Capasso, Z. Gaburro, *Science* **2011**, *334*, 333.

[10] A. V Kildishev, A. Boltasseva, V. M. Shalaev, *Science* **2013**, *339*, 1232009.

[11] A. Boltasseva, H. A. Atwater, *Science* **2011**, *331*, 290.

[12] P. Lalanne, S. Astilean, P. Chavel, E. Cambril, H. Launois, *Opt. Lett.* **1998**, *23*, 1081.

[13] A. Arbabi, Y. Horie, A. J. Ball, M. Bagheri, A. Faraon, *Nat. Commun.* **2015**, *6*, 7069.

[14] A. Arbabi, R. M. Briggs, Y. Horie, M. Bagheri, A. Faraon, *Opt. Express* **2015**, *23*, 33310.

[15] M. Khorasaninejad, W. T. Chen, R. C. Devlin, J. Oh, A. Y. Zhu, F. Capasso, *Science* **2016**, *352*, 1190.

[16] A. Arbabi, E. Arbabi, S. M. Kamali, Y. Horie, S. Han, A. Faraon, *Nat. Commun.* **2016**, *7*, 13682.

[17] Y. Yang, W. Wang, P. Moitra, I. I. Kravchenko, D. P. Briggs, J. Valentine, *Nano Lett.* **2014**, *14*, 1394.

[18] K. E. Chong, I. Staude, A. James, J. Dominguez, S. Liu, S. Campione, G. S. Subramania, T. S. Luk, M. Decker, D. N. Neshev, I. Brener, Y. S. Kivshar, *Nano Lett.* **2015**, *15*, 5369.

[19] Y. F. Yu, A. Y. Zhu, R. Paniagua-Dominguez, Y. H. Fu, B. Luk'yanchuk, A. I. Kuznetsov, *Laser Photon. Rev.* **2015**, *9*, 412.

[20] K. E. Chong, L. Wang, I. Staude, A. R. James, J. Dominguez, S. Liu, G. S. Subramania, M. Decker, D. N. Neshev, I. Brener, Y. S. Kiyshar, *ACS Photonics* **2016**, *3*, 514.

[21] P. R. West, J. L. Stewart, A. V Kildishev, V. M. Shalaev, V. V Shkunov, F. Strohkendl, Y. A. Zakharenkov, R. K. Dodds, R. Byren, *Opt. Express* **2014**, *22*, 26212.

[22] F. Aieta, P. Genevet, M. A. Kats, N. F. Yu, R. Blanchard, Z. Gahurro, F. Capasso, *Nano Lett.* **2012**, *12*, 4932.

[23] M. Khorasaninejad, F. Aieta, P. Kanhaiya, M. A. Kats, P. Genevet, D. Rousso, F. Capasso, *Nano Lett.* **2015**, *15*, 5358.

[24] I. Staude, A. E. Miroshnichenko, M. Decker, N. T. Fofang, S. Liu, E. Gonzales, J. Dominguez, T. S. Luk, D. N. Neshev, I. Brener, Y. Kivshar, *ACS Nano* **2013**, *7*, 7824.

[25] M. Decker, I. Staude, M. Falkner, J. Dominguez, D. N. Neshev, I. Brener, T. Pertsch, Y.

S. Kivshar, *Adv. Opt. Mater.* **2015**, *3*, 813.
[26] O. Akın, H. V. Demir, *Opt. Express* **2015**, *23*, 27020.
[27] A. A. High, R. C. Devlin, A. Dibos, M. Polking, D. S. Wild, J. Perczel, N. P. de Leon, M. D. Lukin, H. Park, *Nature* **2015**, *522*, 192.
[28] Y. Horie, S. Han, J.-Y. Lee, J. Kim, Y. Kim, A. Arbabi, C. Shin, L. Shi, E. Arbabi, S. M. Kamali, H.-S. Lee, S. Hwang, A. Faraon, *Nano Lett.* **2017**, *17*, 3159.
[29] J. P. Hugonin and P. Lalanne, *Reticolo software for grating analysis*, Institut of Optics Graduates School, **2005**.
[30] M.G. Moharam, E.B. Grann, D.A. Pommet, T.K. Gaylord, *J. Opt. Soc. Am. A* **1995**, *12*, 1068.
[31] https://www. lumerical. com. Lumerical Solutions, *Vancouver, Canada* **accessed 2016.**
[32] H. J. Zuo, D. Y. Choi, X. Gai, B. Luther-Davies, B. P. Zhang, *Opt. Express* **2017**, *25*, 3069.
[33] F. Aieta, M. A. Kats, P. Genevet, F. Capasso, *Science*, ***2014***, *347*, 1342.

Supporting Information

High efficiency all-dielectric metalenses for mid-infrared imaging

Haijie Zuo, Duk-Yong Choi, Xin Gai, Pan Ma, Lei Xu, Dragomir N. Neshev, Baoping Zhang, and Barry Luther-Davies*

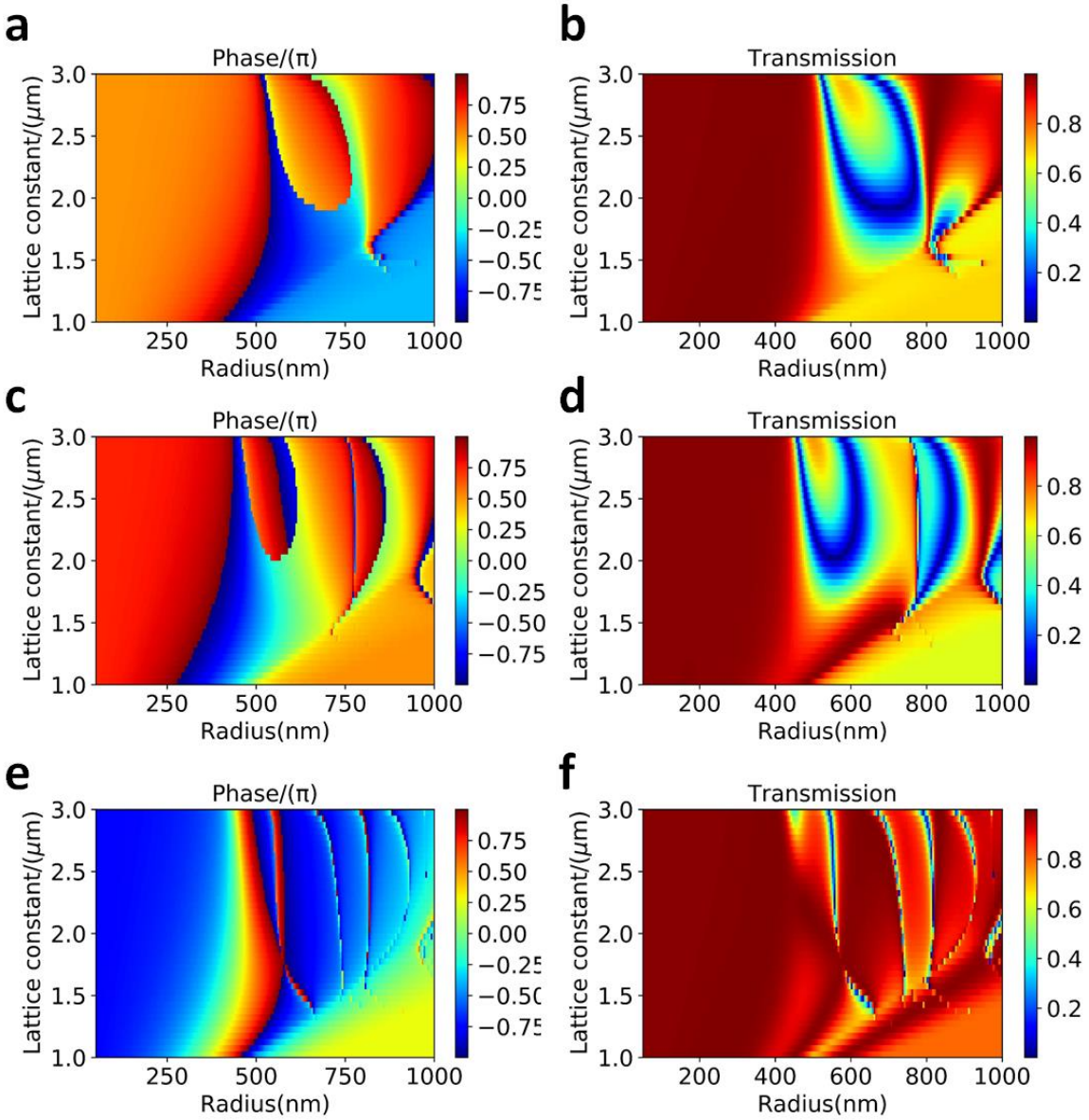

Figure S1. Simulated phase delay and transmission efficiency for NPs as functions of the lattice constant, a, and rod radius, R, for different rod heights: a-b) 1μm, c-d) 1.5μm, e-f) 2.5μm.

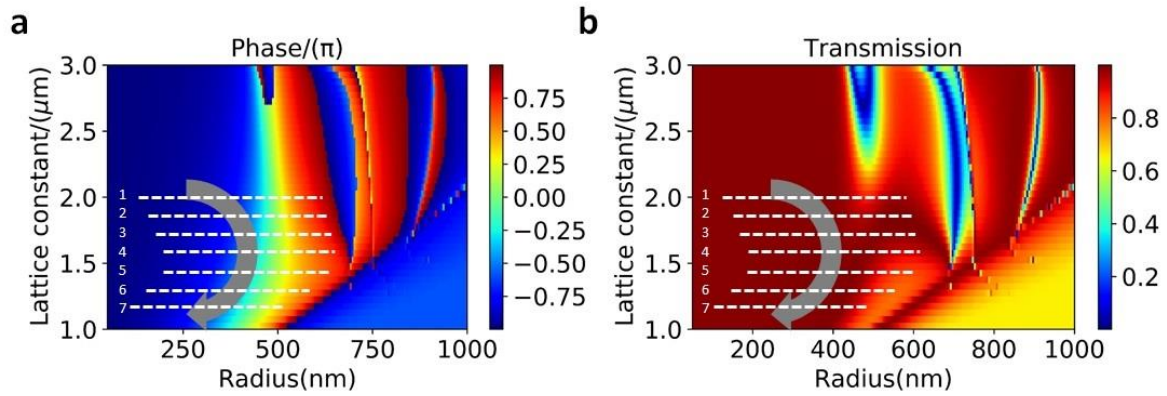

Figure S2. Simulated phase delay (a) and transmission (b) as functions of the lattice constant and NP radius for a NP height of 2μm.

The efficiency drop at larger angles is due to under-sampling of the rapidly varying phase profile that occurs at larger deflection angles, and this can be improved by using a smaller lattice constant. Specifically, as is shown in Figure S2, we can use lattices marked with the dashed lines numbered from 2 to 7 (we applied line 1 in the demonstration), and these can provide sampling resolution from λ/2 down to nearly λ/4. In these cases, the corresponding transmission efficiency remains closer to unity.

Increasing the height of NPs is another approach for obtaining denser arrays. Calculations (see Figure S1 e-f, 2.5μm) show that the rod radius required to achieve 2π phase coverage can then be much smaller, and thus denser arrays can be used using longer rods. To achieve this ICP etching and related wafer processing needs further optimization to achieve the higher aspect ratio that is required.

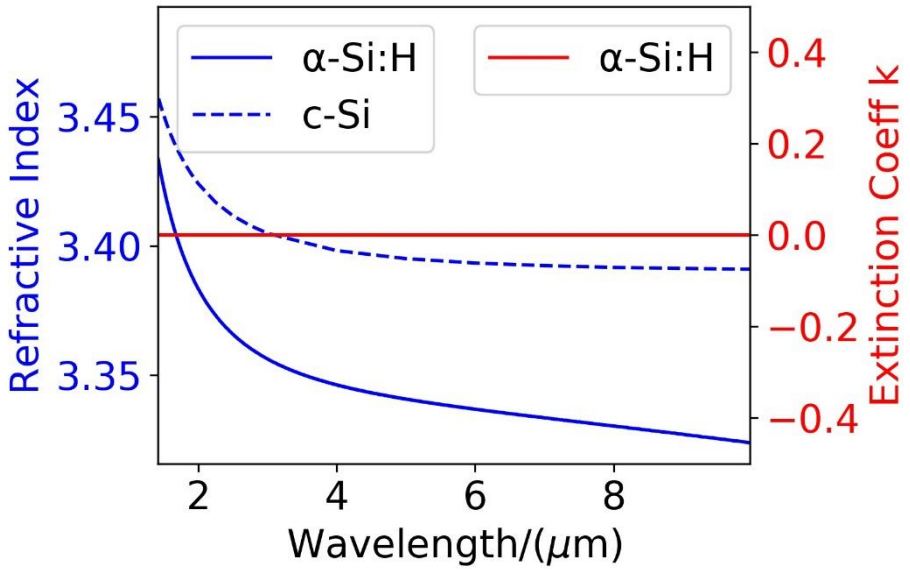

Figure S3. Measured optical coefficients of 2μm α-Si:H using an MIR ellipsometer. The refractive index of silicon was provided for comparison.

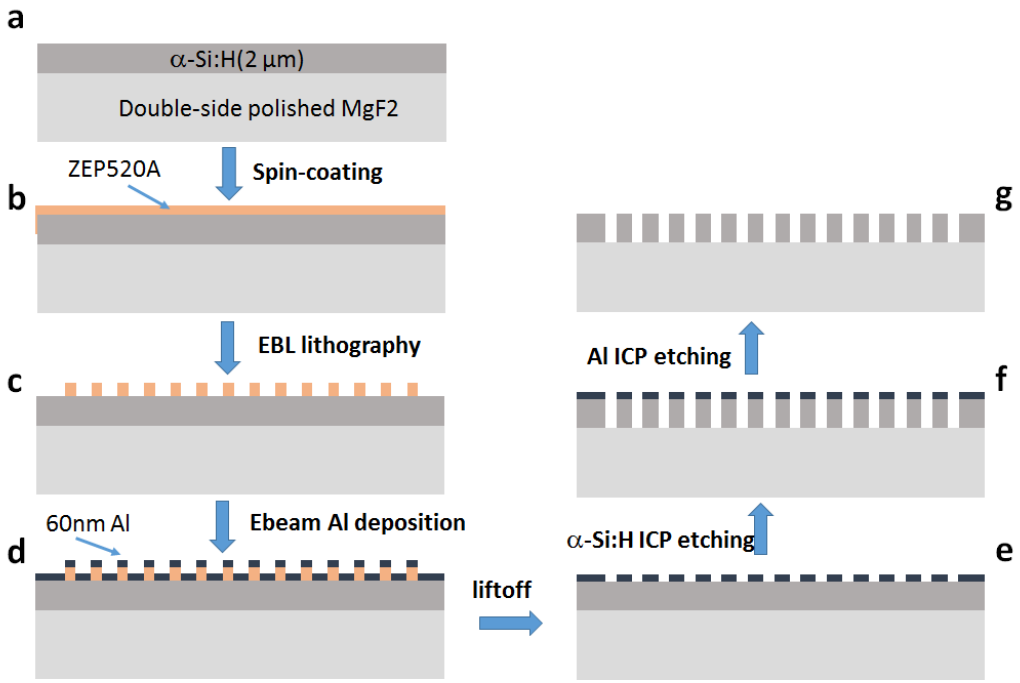

Figure S4. Schematic showing fabrication procedure for the MIR metalenses.

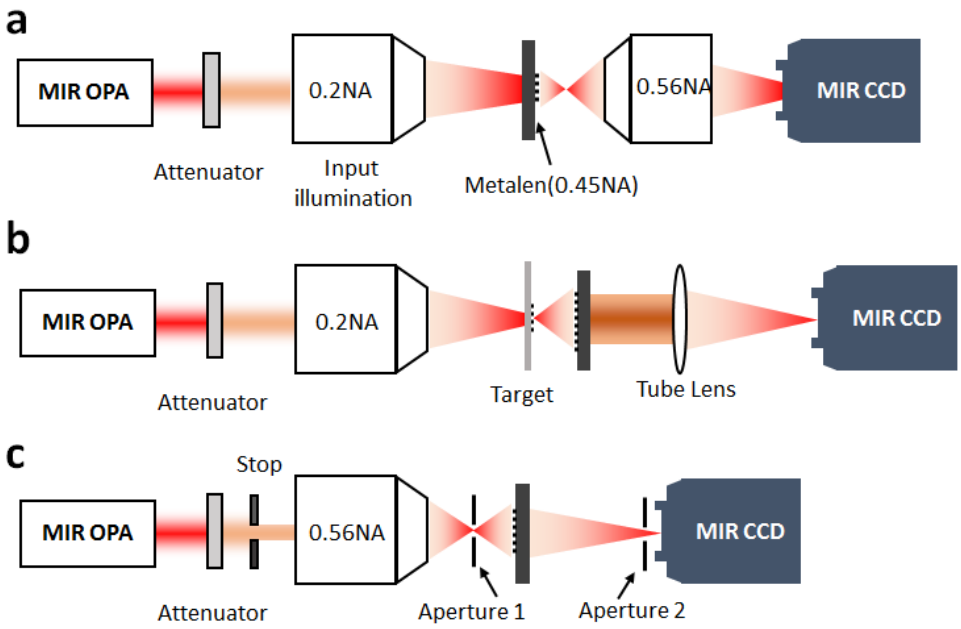

Figure S5. Optical characterization system for the metalens. a) Focal spot measurement. b) Imaging resolution measurement. c) Focusing efficiency measurement.

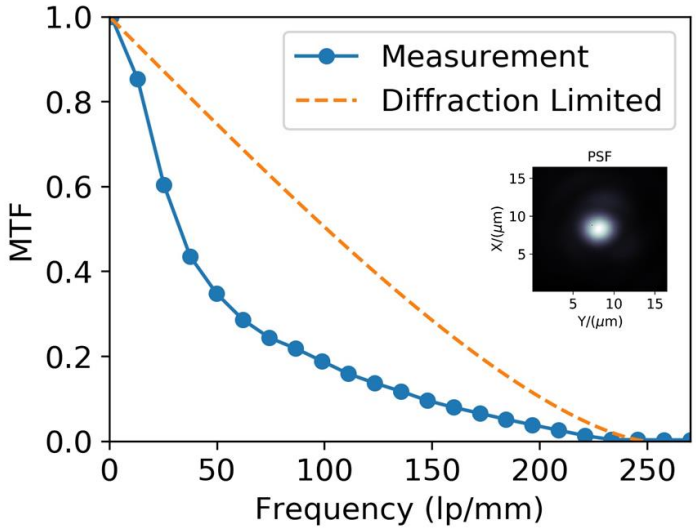

Figure S6. Measured modulation transfer function (MTF) as a function of spatial frequency in line pairs per millimeter (lp/mm). The inset shows the point spread function (PSF) obtained using the setup in Figure S4a, the metalenses was the same one as used in imaging resolution tests and had a NA=0.45.

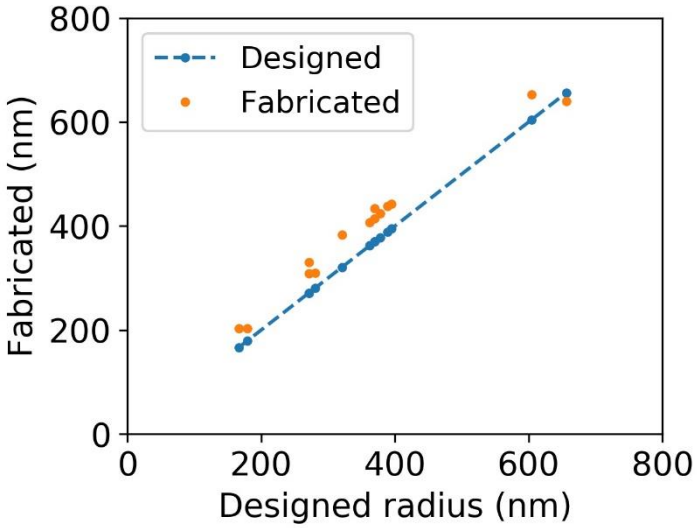

Figure S7. Fabrication errors in the NP radius. The graph indicates that the NP radius was about ~30nm larger than that of the design.